Available online at www.sciencedirect.com
SCIENCE DIRECT®
Journal of Solid State Chemistry 172 (2003) 265–276
JOURNAL OF SOLID STATE CHEMISTRY
http://elsevier.com/locate/jssc

Ternary rare-earth nickel arsenides $R_3Ni_7As_5$ (R = La, Ce, Pr, Nd, Sm) with a new variant of the $BaAl_4$-type: crystal structure and physical properties

V. Babizhetskyy,[a,b,1] R. Guérin,[a,*] O. Isnard,[c,d] and K. Hiebl[b]

[a] *Laboratoire de Chimie du Solide et Inorganique Moléculaire, UMR CNRS 6511, Institut de Chimie, Campus de Beaulieu, Avenue du Général Leclerc, F-35042 Rennes Cedex, France*
[b] *Institut für Physikalische Chemie der Universität Wien, Währingerstrasse 42, A-1090 Wien, Austria*
[c] *Laboratoire de Cristallographie, CNRS associé à l'Université et à l'INPG, Avenue des Martyrs, BP 166X, F-38042 Grenoble Cedex 9, France*
[d] *Institut Universitaire de France, Maison des Universités, 103 Bd Saint Michel, 75005 Paris, France*

Received 8 October 2002; received in revised form 30 December 2002; accepted 10 January 2003

Abstract

The ternary rare-earth nickel arsenides $R_3Ni_7As_5$ (R =La, Ce, Pr, Nd, Sm) were prepared by arc melting the elemental components and subsequent annealing at $T = 1070$ K. The crystal structure of $Ce_3Ni_7As_5$ was determined from single-crystal X-ray data: space group $Pmmn$, $Z = 2$; a =1.24210(6), b =0.40797(2), c =0.96436(5) nm, $R_F = 0.037$ (R_w =0.044); 596 independent reflections; 53 variable parameters. It is a new structure type, which belongs to the family of $BaAl_4$-related structures. The magnetic properties are as follows: $La_3Ni_7As_5$ is a Pauli-type paramagnet above 4.2 K, $Pr_3Ni_7As_5$ remains paramagnetic in the temperature range investigated and $Nd_3Ni_7As_5$ undergoes a ferromagnetic ordering at T_C =24 K. $Sm_3Ni_7As_5$ orders antiferromagnetically at a Néel temperature of T_N =18 K followed by a spin flip towards parallel spin-alignment below T_C =6 K. $Ce_3Ni_7As_5$ reveals a strong deflection of the linear temperature dependence of the inverse susceptibility due to an intermediate valence behavior. The temperature dependence of the electrical resistivities for the La, Pr, Nd, Sm containing samples corroborates with the metallic state of the non-magnetic (La) and the magnetically ordered compounds, whereas in case of $Ce_3Ni_7As_5$ the resistivity seems to be determined by an interplay of Kondo scattering and crystalline field effects. L_{III} X-ray absorption spectra confirm the demagnetization effects owing from valence fluctuations, the actual valence thereby changes from $v = 3.10$–3.14 at room temperature and 10 K, respectively.

Keywords: Ternary rare-earth nickel arsenides; Crystal structure; Electrical transport; Magnetic measurements; X-ray absorption

1. Introduction

A great number of ternary compounds RM_2X_2, where R represents a rare-earth element, M a transition metal and X a non-metal atom (Si, Ge, Sn, As, P, Sb, Bi,…), have been intensively investigated over the last two decades. Most of them crystallize in the well-known $BaAl_4$ derivative structure types $ThCr_2Si_2$ (space group $I4/mmm$) and/or $CaBe_2Ge_2$ (space group $P4/nmm$) [1–3]. In addition, the physical properties of the highly correlated electron systems in case of R being one of the elements Ce, Eu or Yb have been widely studied showing interesting phenomena such as intermediate valence behavior, Kondo effect, heavy fermion superconductivity, Fermi liquid behavior,… [4–6].

In a recent paper, a detailed group-subgroup scheme in the *Bärninghausen* formalism for various ordered and defect variants of the basic $BaAl_4$ type has been presented [7]. Derivatives of the $CaBe_2Ge_2$ type are the distorted structure type $LaPt_2Ge_2$ [8] and several superstructures corresponding either to stoichiometric compounds like $BaMg_2Sn_2$ [9] or non-metal and/or metal deficient ternary compounds such as $Eu_2Au_2Sn_5\square$ [7], $Ce_3Pd_6Sb_5\square$ [10], $Yb_3Au_{5.5}Ga_{5.5}$ [11], $CeNi_{1.91}As_{1.94}$ [12] or $URh_{1.6}As_{1.9}$ [13]. In the same manner, derivatives

*Corresponding author. Laboratoire de Chimie du Solide et Inorganique Moléculaire, UMR CNRS 6511, Institut de Chimie, Avenue du Général Leclerc, F-35042 Rennes Cedex, France. Fax: +33-2-9963-5704.
E-mail address: roland.guerin@univ-rennes1.fr (R. Guérin).
[1] Present address: Max-Planck-Institute, Heisenbergstrasse 1, Postfach 800665, D-70569 Stuttgart, Germany

0022-4596/03/$ - see front matter © 2003 Elsevier Science (USA). All rights reserved.
doi:10.1016/S0022-4596(03)00084-7

of the $ThCr_2Si_2$ type are for example the superstructures of stoichiometric antimonide $BaCu_2Sb_2$ [14] and deficient stannide $Dy_3Co_6Sn_5$ [15].

In the course of our investigations in the Ce–Ni–As system, we have synthesized a ternary phase with orthorhombic symmetry and the approximate formula $Ce_6Ni_{13.4}As_9$ [16]. This phase has also been obtained with R =La and Nd. Unfortunately, we were not able to do the structure determination on single crystals at the time.

During our recent attempts to improve crystal growth of the Ce-containing ternary arsenide by arc melting, we found small single crystals in the form of shiny grey platelets of $Ce_3Ni_7As_5$. The structure determination as well as the investigation of the physical properties of this new ternary compound together with its polycrystalline homologues $R_3Ni_7As_5$ (R =La, Pr, Nd, Sm) are the subject of this paper.

2. Experimental

Polycrystalline samples of the ternary arsenides $R_3Ni_7As_5$ were prepared from pure elements: nickel and amorphous β-As as powders, rare-earth metals as ingots, all supplied with minimum purity 99.9% by Strem Chemicals.

Suitable amounts of powder and freshly filed chips of the constituents in the nominal atomic percentage R:Ni:As = 23:44:33 were mixed together and pressed into pellets. A small excess of arsenic (1 at%) was added to compensate for evaporation losses during the arc melting process. Prior to melting in an arc furnace under Ti/Zr-gettered argon atmosphere, the pellets (about 1 g each) were pre-reacted in evacuated silica tubes by gradually heating them up to 1070 K, kept at this temperature for 2 days and slowly cooled down to room temperature. To ensure homogeneity during the arc melting process, the samples were turned over and re-melted several times. Finally, to reach thermodynamic equilibrium, the so-obtained samples were again sealed in evacuated silica tubes, heated at 1070 K for one month and subsequently quenched in cold water.

Sample characterization was done at first by X-ray diffraction using a powder diffractometer (CPS 120 INEL) equipped with a position-sensitive detector ranging 120° in 2θ. More precise lattice parameters for all ternaries (R =La, Ce, Pr, Nd, Sm) were derived by the least-squares refinements of room temperature Image Plate Huber, G 670 X-ray powder diffractometer data ($8° \leqslant 2\theta \leqslant 100°$, step size = 0.005°) with monochromated Cu$K\alpha_1$ radiation. Elemental germanium (99.9999%, a_{Ge} =0.5657905 nm) served as an internal standard. The unit cell parameters for all compounds $R_3Ni_7As_5$ are given in Table 1.

Shiny grey platelet-like single crystals could be extracted from the Ce-containing molten pellets. They were suitable for structure determination. Energy dispersive analysis of the crystals by a scanning electron microscope confirmed the presence of cerium, nickel and arsenic only. The nominal overall composition in atomic percentage measured by microanalyses on several crystals was found to be Ce:Ni:As = 20.4:45.6:34.1 with standard deviations estimated to be less than 1 at%. It is worthwhile to mention that scanning electron microscopic studies, on bulk samples prepared at 1070 K, revealed the thermodynamic equilibrium between the arsenide $Ce_3Ni_7As_5$ and the ternary compounds $Ce_{20}Ni_{42}As_{31}$ and $Ce_6Ni_{20}As_{13}$ [16]. Single-crystal intensity data were collected at ambient temperature applying a Nonius Kappa CCD X-ray area-detector diffractometer using Mo$K\alpha$ radiation ($\lambda = 0.071073$ nm).

Table 1
Unit cell parameters for the ternary $R_3Ni_7As_5$ arsenides

Compound	a (nm)	b (nm)	c (nm)	V (nm^3)
$La_3Ni_7As_5$	1.2371(2)	0.41765(7)	0.9672(2)	0.4997(3)
$Ce_3Ni_7As_5$[a]	1.24210(6)	0.40797(2)	0.96436(5)	0.48868(4)
$Pr_3Ni_7As_5$	1.2301(2)	0.41217(7)	0.9630(2)	0.4883(3)
$Nd_3Ni_7As_5$	1.2133(2)	0.41002(7)	0.9616(2)	0.4784(3)
$Sm_3Ni_7As_5$	1.2137(6)	0.4102(3)	0.9620(8)	0.4789(8)

[a] Single crystal lattice constants.

Data collection strategy was performed with the help of the program COLLECT [17] and reflections were corrected using the program DENZO of the Kappa CCD software package [18]. Owing to the small size of the single crystals, no absorption correction was necessary. Structures were solved by direct methods (SIR 97 [19]) and least-squares refinements, difference Fourier syntheses were run with the beta version of JANA 2000 [20]. Crystal structure and refinement data are given in Table 2. The program DIAMOND [21] was used to prepare the drawings of the structural units.

The magnetic properties were studied by use of a Faraday balance (SUS-10, A. Paar) in the temperature range 80–900 K and in external fields up to 1.3 T and an AC susceptometer (AC 7000, Lake Shore; f =133.3 Hz; B_{AC} = 1 mT) for temperatures 4.2 K < T < 100 K.

The electrical resistivity measurements were performed applying a common four probe AC resistivity option (Lake Shore; f = 133.3 Hz, i_{AC} = 10 mA) in the temperature range 4.2–300 K. The annealed buttons were cut by a diamond saw (Bühler, Isomet) into bar-shaped samples with the approximate dimensions of ca. $1 \times 1 \times 5\,mm^3$. Electrical contacts were made using commercial silver paints and 25 μm gold wire.

X-ray absorption measurements were performed at the French synchrotron radiation facility of LURE using the X-ray beam delivered by the DCI storage ring, working at 1.85 GeV, ~320 mA, on the extended X-ray absorption fine-structure XAS 13 experimental station. The X-rays were monochromated using two parallel Si

Table 2
Crystal data, intensity collection and refinement for $Ce_3Ni_7As_5$

Empirical formula	$Ce_3Ni_{6.94}As_5$
Crystal system	Orthorhombic
Space group	*Pmmn*
Formula weight ($g\,mol^{-1}$)	1202.42
a (nm)	1.24210(6)
b (nm)	0.40797(2)
c (nm)	0.96436(5)
V (nm^3)	0.48868(4)
Z; density (calc., $g\,cm^{-3}$)	2; 8.19(1)
Crystal size (mm^3)	$0.07 \times 0.04 \times 0.025$
Linear absorption coefficient (mm^{-1})	45.04
θ limits	$1<\theta<37$
Data collected	$-21<h<20$; $-6<k<6$; $-16<l<-16$
Number of measured reflections	2486
Number of independent reflections; $R_{int.}$	$1423[I>1\sigma(I)]$; 0.066
Number of reflections in refinement	$596[I>3\sigma(I)]$
Refined parameters	53
Refinement	F
Unweighted R factor	0.037
Weighted R_w factor $[w^{-1}=\sigma^2(F_o)^2+0.0004F_o^2]$	0.044
Extinction coefficient (*Gaussian isotropic*)	0.0136(4)
Scale factor	0.0602(3)
Goodness-of-fit	1.15
Min/max ($e\text{Å}^{-3}$)	−3.27/3.58

crystals cut along the (311) plane. Rejection of harmonics of order 3 in the Ce L_{III} edge absorption region was achieved by adjusting the parallelism between the two Si crystals. The energy scale was calibrated by reference to the Cr K edge absorption in chromium metal foil. The $Ce_3Ni_7As_5$ sample has been measured at room temperature and in a cryostat kept at a constant temperature of ca. 10 K. The data collection has been performed with a step of 0.3 eV. Room temperature data of the L_{III} edge of cerium have been measured between 5680 and 5820 eV whereas 10 K data have been recorded from 5680 to 5800 eV. The detectors were two ionization chambers filled with air.

For the X-ray absorption data acquisition, the sample $Ce_3Ni_7As_5$ was ground (grain size of 40 μm or smaller). Then a calibrated amount of powder sample was mixed with cellulose in order to optimize the edge jump. This procedure was also used to obtain a homogeneous powder distribution through the sample. All absorption spectra were normalized to the edge jump using the CDXAS software [22].

3. Results and discussion

3.1. Crystal structure

The X-ray structure of $Ce_3Ni_7As_5$ was solved from single-crystal intensity data. Preliminary studies led to the following type of crystal lattice: orthorhombic unit cell, Laue group *mmm*, possible space group *Pmmn, P2₁mn or Pm2₁n* in agreement with the systematic absence of the reflections $h\,k\,l(h+k\neq 2n)$, of which the centrosymmetric space group *Pmmn* appeared to be the correct one during the structure refinement procedure. Crystallographic data and details of data collection are summarized in Table 2.

Table 3
Atomic positional and isotropic displacement parameters for $Ce_3Ni_7As_5$

Atom	Position	Occupancy	x	y	z	[a] $B_{eq.}$ (nm^2)
Ce1	2*a*	1	3/4	3/4	0.7492(1)	72(3)
Ce2	4*f*	1	0.41537(4)	3/4	0.75109(5)	68(2)
Ni1	4*f*	1	0.57904(9)	3/4	0.5034(2)	92(3)
Ni2	2*b*	1	1/4	3/4	0.4920(2)	100(10)
Ni3	4*f*	1	0.4271(1)	3/4	0.1140(2)	86(3)
Ni4	2*b*	1	1/4	3/4	0.0022(2)	121(5)
Ni5	2*a*	0.94(1)	3/4	3/4	0.1425(2)	94(5)
As1	4*f*	1	0.60235(9)	3/4	0.0025(1)	101(3)
As2	4*f*	1	0.41797(7)	3/4	0.3621(1)	75(2)
As3	2*a*	1	3/4	3/4	0.3803(2)	78(4)

[a] $B_{eq}=1/3[B_{11}a^{*2}a^2+\cdots.2B_{23}b^*c^*bc\cos(\alpha)]$.

The atomic parameters were deduced from interpretation of direct methods and the structure was then refined very smoothly in order to make a correct identification of the nickel and arsenic positions with respect to the known interatomic distances. Including isotropic displacement parameters during the refinement cycles, the filling of the position 2*a* ($z=0.1425$) with nickel instead of arsenic, namely with the Ni5 atom, was consistent with an accurate displacement parameter, together with improbable As–As distances of 0.228 nm. This Ni5 position presents a slight deficit ($\tau=0.94(1)$). Final refinements including anisotropic displacement parameters converged to the reliability factors given in Table 2. The final difference Fourier synthesis did not reveal significant residual peaks. Atomic positional and displacement parameters are listed in Table 3 and selected interatomic distances are given in Table 4. The crystallographic data can be obtained from the FIZ Karlsruhe under the CSD-number 412889. The final formula of this arsenide, as deduced from the structure refinement, is therefore $Ce_3Ni_{6.94}As_5$, leading to the atomic proportions Ce:Ni:As = 20.08:46.45:33.47. This result is in good accord with the electron probe microanalyses (20.4:45.6:34.1).

The structure of $Ce_3Ni_7As_5$ exhibits a new structure type, which belongs to the family of $BaAl_4$-related structures. As the atomic composition is slightly different from 1:2:2, that means that only parts of the $Ce_3Ni_7As_5$ structure can be related to one of the well-known $ThCr_2Si_2$ or $CaBe_2Ge_2$ structure types (2, 3). The 3D representation of the $Ce_3Ni_7As_5$ structure, as shown in Fig. 1, is compared with the one of the $CaBe_2Ge_2$

Table 4
Main interatomic distances (nm) for $Ce_3Ni_7As_5$ and estimated standard deviations

Ce1–2 As1	0.3055(1)	Ni1–2 As2	0.2417(1)
Ce1–2 Ni2	0.3094(2)	Ni1–1 As2	0.2421(2)
Ce1–4 As2	0.3109(1)	Ni1–1 As3	0.2433(2)
Ce1–2 Ni4	0.3148(2)	Ni1–2 Ni1	0.2832(1)
Ce1–2 Ni1	0.3182(2)	Ni1–2 Ni2	0.2945(1)
Ce1–4 Ni3	0.3277(1)	Ni1–1 Ce2	0.3136(2)
		Ni1–1 Ce1	0.3182(2)
Ce2–2 Ni5	0.3071(1)	Ni1–2 Ce2	0.3193(2)
Ce2–2 As2	0.3105(1)		
Ce2–2 Ni3	0.3111(1)	Ni2–2 As3	0.2382(2)
Ce2–1 Ni1	0.3136(2)	Ni2–2 As2	0.2434(2)
Ce2–2 As1	0.3139(1)	Ni2–4 Ni1	0.2945(1)
Ce2–2 As3	0.3160(1)	Ni2–2 Ce1	0.3094(2)
Ce2–1 Ni4	0.3175(2)	Ni2–2 Ce2	0.3234(2)
Ce2–2 Ni1	0.3193(2)		
Ce2–1 Ni2	0.3234(2)	Ni3–2 As1	0.2358(1)
Ce2–1 As1	0.3358(2)	Ni3–1 As2	0.2396(2)
		Ni3–1 As1	0.2428(2)
As1–1 Ni5	0.2277(2)	Ni3–1 Ni4	0.2449(2)
As1–2 Ni3	0.2357(1)	Ni3–2 Ce2	0.3112(1)
As1–1 Ni3	0.2428(2)	Ni3–2 Ce1	0.3277(1)
As1–2 Ni4	0.2743(1)		
As1–1 Ce1	0.3054(1)	Ni4–2 Ni3	0.2449(2)
As1–2 Ce2	0.3139(1)	Ni4–2 Ni5	0.2472(2)
As1–2 As1	0.3260(2)	Ni4–4 As1	0.2743(1)
As1–1 Ce2	0.3358(2)	Ni4–2 Ce1	0.3148(2)
		Ni4–2 Ce2	0.3175(2)
As2–1Ni3	0.2396(2)		
As2–2 Ni1	0.2416(1)	Ni5–2 As1	0.2277(2)
As2–1 Ni1	0.2421(2)	Ni5–1 As3	0.2293(3)
As2–1 Ni2	0.2433(2)	Ni5–2 Ni4	0.2472(2)
As2–2 Ce2	0.3105(1)	Ni5–4 Ce2	0.3071(1)
As2–2 Ce1	0.3109(1)		
As3–1 Ni5	0.2293(3)		
As3–2 Ni2	0.2382(2)		
As3–2 Ni1	0.2433(2)		
As3–4 Ce2	0.3160(1)		

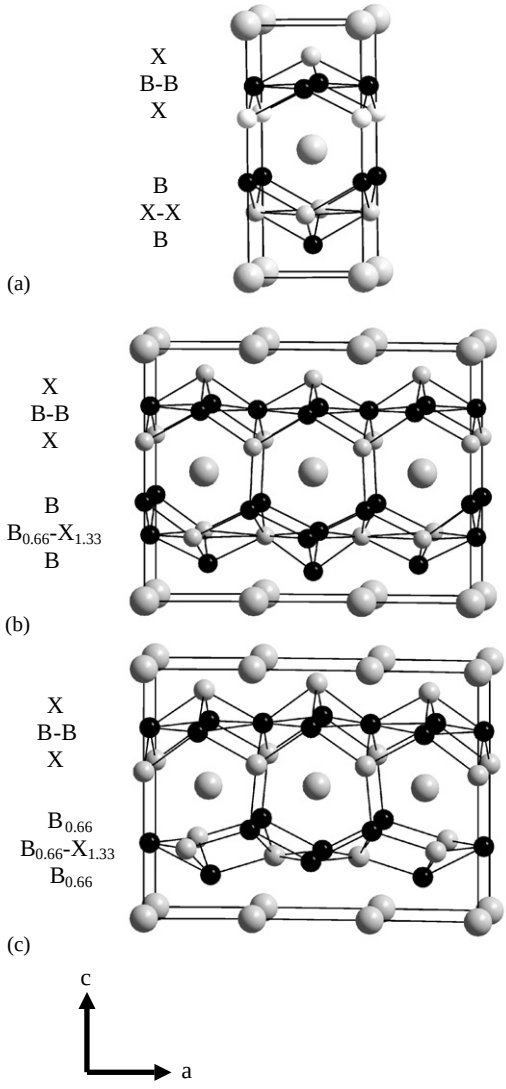

Fig. 1. Structural relationship between (a) $CaBe_2Ge_2$, (b) $Ce_3Ni_7As_5$ and (c) $Ce_3Pd_6Sb_5$. The origin of the structures have been shifted for a better comparison. The B_2X_2 layers have been emphasized. Black and white spheres within the layers correspond to the transition metal and the metalloid atoms, respectively.

type. One can see that the structure of $Ce_3Ni_7As_5$ is built up from three pseudo-body-centered subcells formed by the cerium atoms with regard to the *a* parameter of the $Ce_3Ni_7As_5$ unit cell, which is three times larger than the unit cell of $CaBe_2Ge_2$.

Another similar superstructure has been also observed for the defective ternary antimonide $Ce_3Pd_6Sb_5$, into which a non-metal vacancy *a priori* modifies the expected composition 1:2:2 [10]. Indeed, the crystal structure of this antimonide is closely related to the one of $Ce_3Ni_7As_5$. First, the unit cell parameters $a = 1.3481(2)$, $b = 0.4459(1)$, $c = 1.0050(1)$ nm are of the same order of magnitude than those of the ternary arsenide (Table 1) and furthermore the crystal structure of $Ce_3Pd_6Sb_5$ has been also described in space group *Pmmn,* with atomic coordinates close to the ones found for $Ce_3Ni_7As_5$. However, the compositional change from $Ce_3Ni_7As_5$ to $Ce_3Pd_6Sb_5$ shows that, in fact, the $Ce_3Pd_6Sb_5$ structure exhibits a metal defect with respect the one of $Ce_3Ni_7As_5$ (Fig. 1c).

A thorough examination of the prototypes $ThCr_2Si_2$ and $CaBe_2Ge_2$ shows the occurrence of two sheets B_2X_2 per cell (B =Cr, Be; X =Si, Ge) interspersed with layers of larger metal atoms (Th or Ca). While the spatial distribution within the sheets is always *XBBX* in the $ThCr_2Si_2$ type, alternating *XBBX* and *BXXB* sequences occur in the $CaBe_2Ge_2$ type. This atomic distribution generates Si–Si pairs in $ThCr_2Si_2$, whereas no Ge–Ge bonding occurs in $CaBe_2Ge_2$. The structural relationship between $Ce_3Ni_7As_5$ and $CaBe_2Ge_2$ (Fig. 1a and b) shows that the XBBX sheet remains unchanged in both structures, contrary to the *BXXB* one, which is strongly

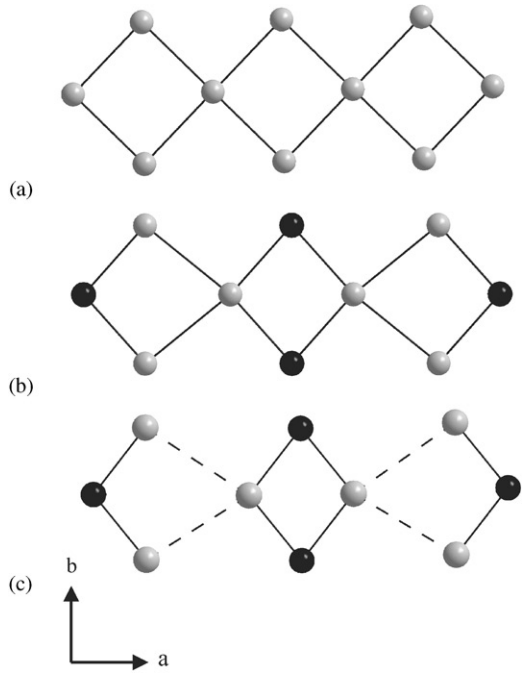

Fig. 2. Representation in the (001) plane: (a) infinite and regular subnet formed by the Ge atoms within the $B[XX]B$ layer in the $CaBe_2Ge_2$ structure, (b) and (c) infinite and distorted subnet formed by metalloïd and transition metal atoms within the same layer in the structures of $Ce_3Ni_7As_5$ and $Ce_3Pd_6Sb_5$, respectively. Black and white spheres correspond to the metal (Ni or Pd) and the metalloid (As or Sb or Ge) atoms, respectively.

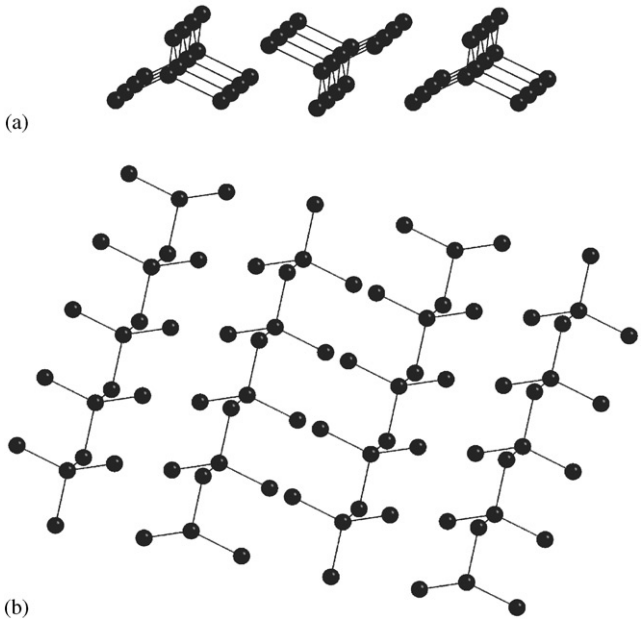

Fig. 3. Representation of the Ni–Ni bonds developing infinite zigzag chains in an alternating manner in the $Ce_3Ni_7As_5$ structure: (a) along the [010] direction and (b) in projection on the (001) plane.

modified. Indeed, in the *ab* plane normally occupied by the *X* atoms within the sheet $B[XX]B$ in $CaBe_2Ge_2$ (Fig. 2a), one can see the substitution of one third of the *X* atoms by the *B* atoms in $Ce_3Ni_7As_5$ (Fig. 2b), which leads to a new sheet that can be labelled as $B[B_{0.66}X_{1.33}]B$. As a consequence, this substitution induces atomic displacements within the overall sheet in $Ce_3Ni_7As_5$, that are still more pronounced in the case of $Ce_3Pd_6Sb_5$ (Fig. 2c). In this structure, apart from this deformation, one can see that one third of the *B* atoms on both sides of the sheet has been removed, leading to metal vacancies (Fig. 1c). Therefore, the corresponding sheet can be labelled as $B_{0.66}[B_{0.66}X_{1.33}]B_{0.66}$ in $Ce_3Pd_6Sb_5$. Finally, the structures $Ce_3Ni_7As_5$ and $Ce_3Pd_6Sb_5$, which are truly both derivatives from the $CaBe_2Ge_2$ type, are structurally related in a way that $Ce_3Ni_7As_5$ is in fact a filled-up $Ce_3Pd_6Sb_5$ structure.

A more detailed analysis of the $Ce_3Ni_7As_5$ structure shows that cerium occupies two different crystallographic positions. The Ce1 atom is surrounded by six arsenic and ten nickel atoms, while the Ce2 one has six arsenic and nine nickel neighbors. The Ni1 and Ni2 atoms within the *XBBX* sheet occupy arsenic tetrahedra, as expected, while the Ni3, Ni4 and Ni5 atoms, lying in the sheet $B[B_{0.66}X_{1.33}]B$, exhibit unusual As coordination numbers of three for the Ni3 and Ni5 and four atoms for the Ni4 atoms, respectively. The Ni–As distances, comprised between 0.228 and 0.274 nm are indicative of atomic displacements in the layer (vide supra). In this structure, no As–As bonding occurs since the shortest distances exceed 0.32 nm.

The main structural characteristic of $Ce_3Ni_7As_5$ results from the establishment of strong Ni–Ni bonds, within the layer $B[B_{0.66}X_{1.33}]B$. These bonds, generated by the Ni4 and Ni5 atoms, develop infinite zig-zag chains along the [010] direction. Moreover, each Ni4 atom within the chain is linked to two apical Ni3 atoms, that induces finally alternating up and down chains (Fig. 3). The Ni4–Ni5 distances of 0.247 nm within the chain (angle Ni4–Ni5–Ni4 = 111.22°) are of the same order of magnitude than the Ni3–Ni4 ones of 0.245 nm outside the chain (angle Ni3–Ni4–Ni3 = 127.77°). These Ni–Ni distances compare well with twice the metallic radius of nickel for CN 12 of 0.248 nm [23]. It is evident that these metal-metal bonds result from the atomic displacements within the sheet $B[B_{0.66}X_{1.33}]B$. Contrary, due to the metal defect, the structure $Ce_3Pd_6Sb_5$ shows only triangular Pd_3 units with Pd3–Pd4 distances of 0.276 nm (angle Pd3–Pd4–Pd3 = 125.78°) (Fig. 1c).

Such Ni–Ni bonds, forming infinite chains, have been previously found in literature. It can be noted that infinite linear chains are present in the prototype NiAs structure (Ni–Ni = 0.2518 nm) [24], while infinite zig-zag chains occur in the binary NiP (Ni–Ni = 0.2532 nm) [25]. Moreover the zig-zag chains are not independent since they are linked through additional Ni–Ni bonds of 0.2756 nm. Another example is that of $Ce_{16}Ni_{36}P_{22}$,

where the Ni atoms aggregate as octahedral clusters (Ni–Ni = 0.243 nm), around the sixfold axis of the hexagonal unit cell [26].

3.2. Magnetic properties

The magnetic properties of the $R_3Ni_7As_5$ (R = La → Sm) were investigated in the temperature range 4.2 K < T < 900 K and in external fields up to 1.3 T. They are presented in Figs. 4–7 and listed in Table 5. $La_3Ni_7As_5$ is a weak Pauli-type paramagnet in the temperature range between 4.2 K and room temperature. The measured values of the susceptibility at room temperature and 4.2 K were found to be $\chi(300\,K) = 0.9 \times 10^{-8}\,m^3/kg$ and $\chi(4.2\,K) = 15 \times 10^{-8}\,m^3/kg$, respectively. The increase of χ at low temperatures ($T < 20$ K) has to be attributed to impurities.

The susceptibilities of the $R_3Ni_7As_5$ (R = Pr → Sm) follow a modified Curie–Weiss law for temperatures above 50 K,

$$c = \frac{C}{T - \Theta_p} + \chi_0 \quad (1)$$

C being the Curie constant, Θ_p is the paramagnetic Curie temperature and χ_0 denotes temperature independent contributions such as core diamagnetism, Landau diamagnetism and Pauli paramagnetism (Figs. 4–6). The calculated values of the effective moments are in good accord with the tripositive theoretical ones for Pr and Nd, respectively. The Sm containing compound is expected to show the characteristic Van Vleck type of paramagnetism owing to the low lying multiplets, however this sample was only measured in a limited temperature range below 100 K and hence the derived magnetic values must be treated with caution. $Pr_3Ni_7As_5$ remains paramagnetic down to the temperature of liquid helium as can be seen from the inset of Fig. 4. Upon lowering the temperatures below 30 K, the latter two

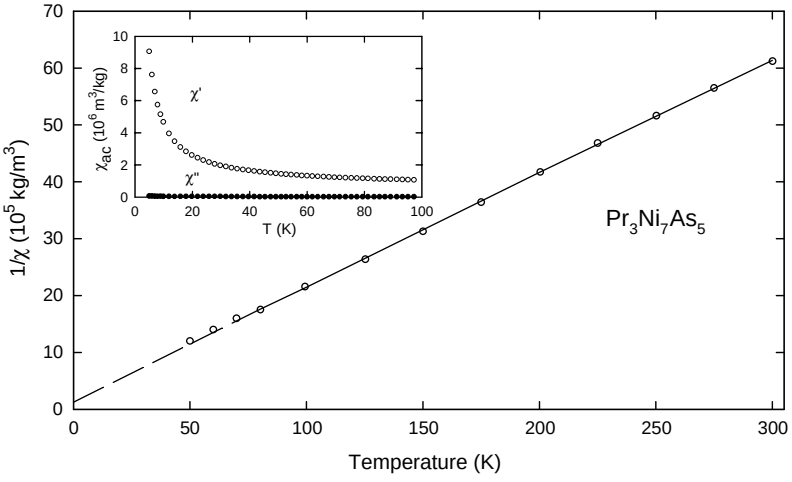

Fig. 4. Reciprocal susceptibility versus temperature for $Pr_3Ni_7As_5$. Inset: AC susceptibility versus temperature.

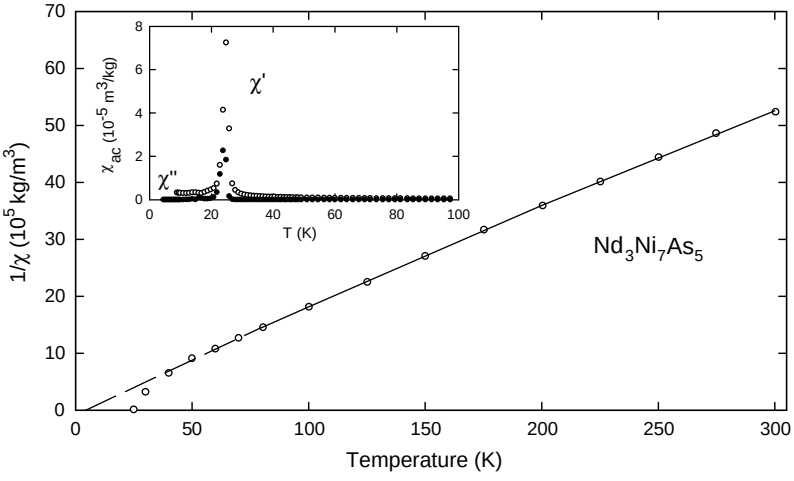

Fig. 5. Reciprocal susceptibility versus temperature for $Nd_3Ni_7As_5$. Inset: AC susceptibility versus temperature.

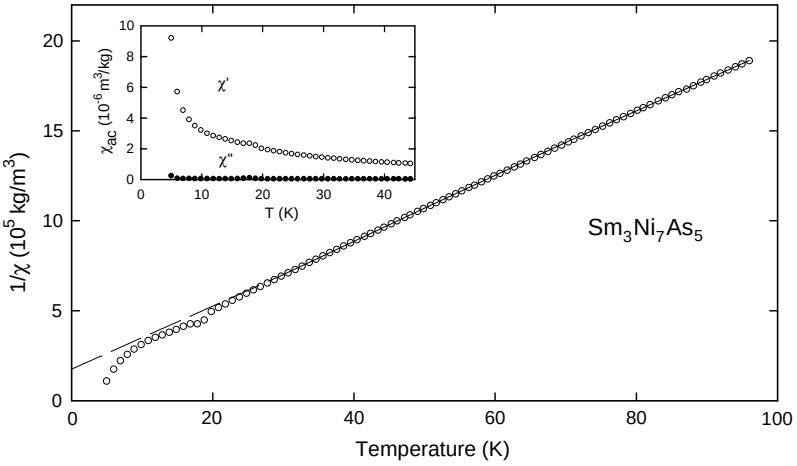

Fig. 6. Reciprocal susceptibility versus temperature for $Sm_3Ni_7As_5$. Inset: AC susceptibility versus temperature.

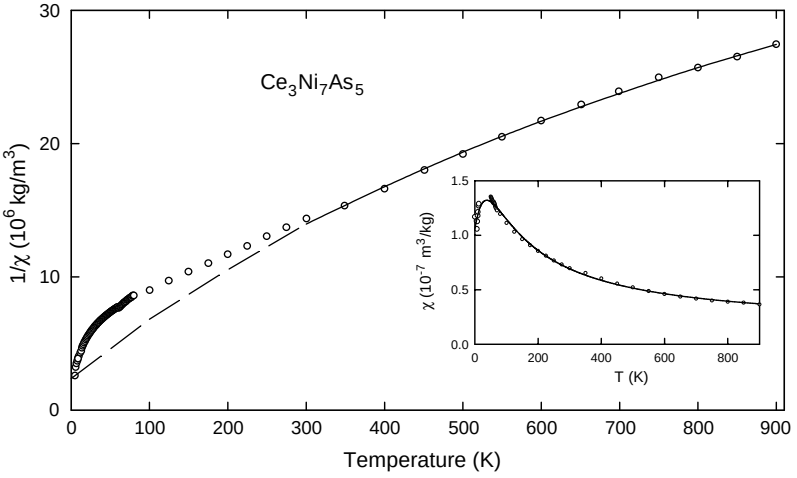

Fig. 7. Reciprocal susceptibility versus temperature for $Ce_3Ni_7As_5$. Inset: corrected susceptibility data versus temperature according to Eq. (2). Solid line: least-squares fit according to Eqs. (3) and (4).

Table 5
Magnetic and electric data for ternary compounds $R_3Ni_7As_5$

Compound	μ_{eff} (μ_B)	Θ_p (K)	T_N (K)	T_C (K)	$d\rho/dT$ (K)	α
$La_3Ni_7As_5$	$\chi_{(300\,K)} = 0.9 \times 10^{-8}\,m^3/kg$, $\chi_{(1.8\,K)} = 15 \times 10^{-8}\,m^3/kg$					
$Ce_3Ni_7As_5$	2.30(5)	−53(3)	—	—	—	—
$Pr_3Ni_7As_5$	3.50(5)	−6(1)		—	—	—
$Nd_3Ni_7As_5$	3.60(5)	4(1)	—	24	23	3
$Sm_3Ni_7As_5$	(3.80(5))	−10(2)	18	6	17, 7	4, 2

arsenides undergo magnetic ordering. In case of $Nd_3Ni_7As_5$, both plots of the dynamic susceptibilities versus temperature exhibit pronounced maxima at $T_C = 24\,K$ as can be seen from the inset of Fig. 5 suggesting a ferromagnetic ground state of the neodymium sublattice. A positive value of Θ_p confirms this assumption. The χ_{AC} versus T plots for $Sm_3Ni_7As_5$ (inset Fig. 6) reveal several features: the real part $\chi'(T)$ passes a soft shoulder at $T_N = 18\,K$ and is followed by a strong increase below $T_C = 6\,K$, whereas the imaginary part $\chi''(T)$ remains temperature independent down to 6 K and rises below that temperature. Hence we conclude that Sm spin system first undergoes an antiferromagnetic ordering followed by a spin flop at 6 K towards a parallel spin alignment (ferromagnetism). A negative value of Θ_p supports this argument. We

point out that these observations corroborate with the findings in the measurements of the electrical resistivity (vide infra).

The compound $Ce_3Ni_7As_5$ remains paramagnetic down to 4.2 K. The reciprocal susceptibility versus temperature plot, however, remarkably deflects from the quasilinear Curie–Weiss behavior for temperatures below 350 K (Fig. 7). The moment calculation according Eq. (1) in the high temperature regime results in $\mu_{eff} = 2.27\,\mu_B$ ($\mu_{eff}^{theor} = 2.54\,\mu_B$ for Ce^{3+}) and a "medium-large" negative value of $\Theta_p = -53$ K. Such an experimental finding is reminiscent of the peculiar magnetic behavior of intermediate valence (IV) systems. Below ~ 50 K, however, the $1/\chi$ values decrease more rapidly instead of tending to a constant value as could be expected for IV compounds. This observation is frequently found in cerium-based materials and commonly attributed to the presence of small amounts of impurities, e.g., oxides of cerium… [27–29]. To account for this impurity contributions, we followed the procedure employed by Béal–Monod and Lawrence [27]. Neglecting crystal-field effects on impurity sites, we assumed that at sufficiently low temperatures the measured susceptibility can be expressed as

$$\chi(T \to 0) = \chi(0) + \frac{C_{imp}}{T}, \tag{2}$$

where $\chi(0)$ denotes the intrinsic susceptibility of an IV compound at $T = 0$ K, and C_{imp} is the Curie constant of impurity magnetic moments. If the impurity contribution is only composed of stable Ce^{3+} ions, an impurity concentration $n = C_{imp}/C$, where $C = 1.014 \times 10^{-5}$ m^3/mol K is the Curie constant of free Ce^{3+} ions. Fitting the experimental data for $T < 50$ K to Eq. (2) yielded the following parameters: $\chi(0) = 4.7 \times 10^{-8}$ m^3/mol and $n = 5.0 \times 10^{-2}$ Ce atom/mol. Finally the $\chi(T)$ dependencies were corrected for impurities subtracting the term nC/T from the experimental data in the whole temperature range studied. The so-corrected $\chi(T)$ curve is displayed in the inset of Fig. 7.

A possible approach describing the features of an intermediate-valence system is the interconfiguration fluctuation (ICF) model developed by Sales and Wohlleben [30]. Within the scope of this model the magnetic susceptibility of a IV cerium compound is given by

$$\chi(T) = \frac{N\mu_{eff}^2[1 - v(T)]}{3k_B(T + T_{SF})} + \chi_0, \tag{3}$$

where $\mu_{eff} = 2.54\,\mu_B$ is the effective magnetic moment of the cerium $4f^1$ state, T_{SF} denotes a characteristic temperature associated with fluctuations between the $4f^0$ and $4f^1$ states due to interactions with conduction electrons, χ_0 accounts for possible conduction-electron paramagnetic and core diamagnetic as well as for the temperature independent Van Vleck contribution to the total measured magnetic susceptibility, while $v(T)$ stands for mean occupation of the ground state. This fractional valence is temperature and energy dependent via the relation

$$n(T) = \frac{1}{1 + 6\exp[-E_{ex}/k_B(T + T_{SF})]}, \tag{4}$$

where E_{ex} is the energy difference between the $4f^1$ and the $4f^0$ states. It appears that this ICF model seems to describe quite well the magnetic behavior of $Ce_3Ni_7As_5$ in the temperature range above 50 K. The least-squares fit of the experimental $\chi(T)$ variations is shown in the inset of Fig. 7 by the solid line; the fitting parameters are: $E_{ex}/k_B = 194$ K, $T_{SF} = 65$ K and $\chi_0 = 6.2 \times 10^{-9}$ m^3/mol. Then, from Eq. (4) it is possible to estimate the temperature dependence of the cerium atom valence. A strong increase of the effective valence is observed from 3.17 at 900 K, down to 3.26 at 200 K, 3.35 at 100 K and 3.68 at 10 K. The latter value has to be taken with care, since the susceptibility does not obey the ICF model below ~ 50 K and furthermore a total depopulation of the $4f^1$ is not likely to occur in this compound. Absolute values of the valence, which are considered to be more reliable, have been derived from L_{III} absorption data below (we note that the valence of Ce in metallic compounds does not exceed 3.4 from X-ray absorption data).

3.3. Electrical resistivity

The results of the electrical resistivity versus temperature for the samples $R_3Ni_7As_5$ (R = La → Sm) are presented in Figs. 8 and 9. The $\rho(T)$ curve for $La_3Ni_7As_5$ resembles the typical shape of a metal-like intermetallic compound. Assuming the validity of Mathiesen's rule, the resistivity of a nonmagnetic compound follows the Bloch–Grüneisen relation [31,32]

$$\rho(T) = \rho_0 + 4R\Theta_D\left(\frac{T}{\Theta_D}\right)^5 \times \int_0^{\Theta_D/T} \frac{x^5\,dx}{(e^x - 1)(1 - e^{-x})} - KT^3. \tag{5}$$

We have fitted our data according Eq. (5) with the following results: residual resistivity ($\rho_0 = 80\,\mu\Omega$ cm), the second, phonon scattering term ρ_{ph} ($R = 0.55\,\mu\Omega$ cm/K; the Debye-temperature $\Theta_D = 176$ K is a rather low value, indicating a soft lattice, and should therefore be proved by specific heat measurements) and the third term, which is due to the scattering of the conduction electrons into a narrow d-band near the Fermi level ($K = 1.39 \times 10^{-6}\,\mu\Omega$ cm/K^3).

The temperature dependence of the resistivity of $Ce_3Ni_7As_5$ as shown in Fig. 8 reveals the typical shape of an intermetallic compound exhibiting spin fluctuations due to Kondo interactions [33], for

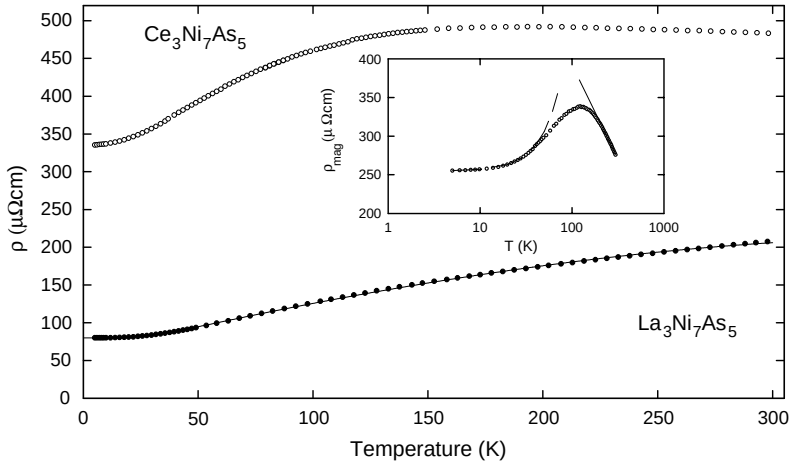

Fig. 8. Electrical resistivity versus temperature for $La_3Ni_7As_5$ (solid line least-squares fit according to Eq. (5)), as well as for $Ce_3Ni_7As_5$. Inset: $\rho_{mag}(T)$ derived after Eq. (6), solid lines calculated according to Eq. (7) dashed line calculated after $\rho = \rho_0 + AT^2$.

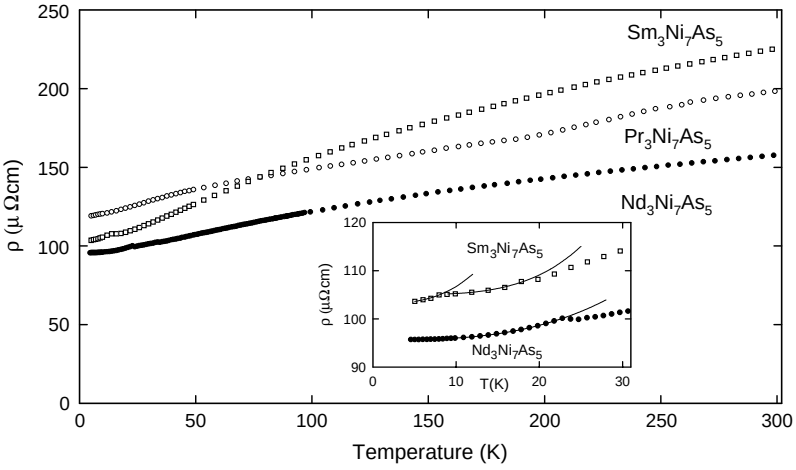

Fig. 9. Electrical resistivity versus temperature for $Pr_3Ni_7As_5$, $Nd_3Ni_7As_5$ and $Sm_3Ni_7As_5$. Inset: $\rho(T)$ near the ordering temperatures, solid lines calculated according to $\rho = \rho_0 + aT^{\alpha}$.

example, well-known heavy fermion systems UPt_3 [34], UNi_2Al_3 [35], or $CeAl_3$ and $CeCu_2Si_2$ [36] or many rare-earth and actinoid Laves phases [37] with an archetypal spin fluctuator UAl_2 [38]. The resistivity starts to rise below room temperature, passes a wide maximum between 200 and 100 K, decreases then smoothly and levels off below 20 K. The room temperature value of about 480 μΩ cm thereby is a standard value for narrow f-band materials. Assuming that the resistivity of the lanthanum-based homologue can be taken as a good approximation of the phonon contribution to the total measured resistivity of $Ce_3Ni_7As_5$, we expressed $\rho(T)$ for this compound as follows:

$$\rho(T) = \rho_0 + \rho(La_3Ni_7As_5) - \rho_0(La_3Ni_7As_5) + \rho_{mag}(T) \quad (6)$$

and in this way extracted the temperature dependence of the magnetic scattering resistivity which is displayed in the inset of Fig. 8. It is apparent from the inset of Fig. 8 that at elevated temperatures the magnetic contribution to the resistivity of $Ce_3Ni_7As_5$ exhibits a pronounced logarithmic decrease with rising temperature, which could be described by Kondo-type interactions of the conduction electrons with the localized cerium magnetic moments. The fit of $\rho_{mag}(T)$ for $T > 100$ K to the standard formula [39]

$$\rho_{mag}(T) = \rho_0^{\infty} - c_K \ln(T) \quad (7)$$

yielded a value of 879 μΩ cm for the spin disorder resistivity ρ_0^{∞} and 106 μΩ cm for the Kondo coefficient c_K. In the scope of the theory by Kondo [39], c_K is proportional to the electronic density of states at the Fermi energy $N(E_F)$. Thus, the rather large Kondo

coefficient derived may indicate strongly enhanced $N(E_F)$ making this compound a good candidate for heavy fermion research. It is known [40] that the electronic ground state of a dense Kondo system is a Fermi liquid and hence the electrical resistivity should vary at low temperatures according to T^2 law, which is indeed the case for this compound in the temperature range $4.2\,K < T < 50\,K$ as shown in the inset of Fig. 8. The coefficient A in the T^2 term is inversely proportional to the square of the Kondo temperature T_K [41]. Moreover, according to the scaling found by Kadowaki and Woods [42] for existing heavy fermion compounds, the constant A is related to the electronic coefficient of the specific heat γ via the universal ratio

$$A/\gamma^2 = 1.0 \times 10^{-5}\,\mu\Omega\,cm\,K^2\,mol^2/mJ^2. \quad (8)$$

However the parameter A is equal to $0.0204\,\mu\Omega\,cm/K^2$ thus yielding from Eq. (8) a rather moderate γ value of about $45\,mJ/mol\ K^2$ only. Since this latter value is obviously a very crude estimate of γ, we propose to investigate this intriguing compound by specific heat measurements down in the mK regime in the near future to shed more light on its low-temperature electronic properties.

The temperature dependencies of the resistivities for the remaining compounds $R_3Ni_7As_5$ (R = Pr, Nd and Sm) as shown in Fig. 9 resemble the shape of metal-like, magnetically ordered intermetallics. The values of $\rho(T)$ decrease with decreasing temperature with a change of slope at the magnetic ordering temperature due to the reduction in scattering of the conduction electrons in the ordered state. The extrema of the first derivative $d\rho/dT$ thereby are in good accord with the magnetically derived values above (Table 5). Furthermore the resistivities approximately scale with T^α terms as predicted for isotropic ferro- and antiferro-magnets. The parameters α are also listed in Table 5.

3.4. X-ray absorption spectroscopy

Results of X-ray absorption spectroscopy are shown in Fig. 10 for the data recorded at 10 K and 300 K, respectively. It can be seen that the spectra show a double peak structure, characteristic for an intermediate valence state of the Ce atoms. The spectra observed in Fig. 11 exhibit two resolved peaks separated by about 10 eV. These peaks are due to optical transitions from a $2p_{3/2}$ electron to an empty $5d$ state in the presence of two different occupancies of the $4f$ shell ($4f^0$ and $4f^1$) in the final state. It has been shown that, provided the different Coulomb interactions between the photoelectron and the system are taken into account, the L_{III}, L_{II} absorption edges give a relevant representation of the electronic configuration in the ground state and yielded the $4f$ occupation number [43,44]. In order to make a more quantitative estimation of the Ce valence state we

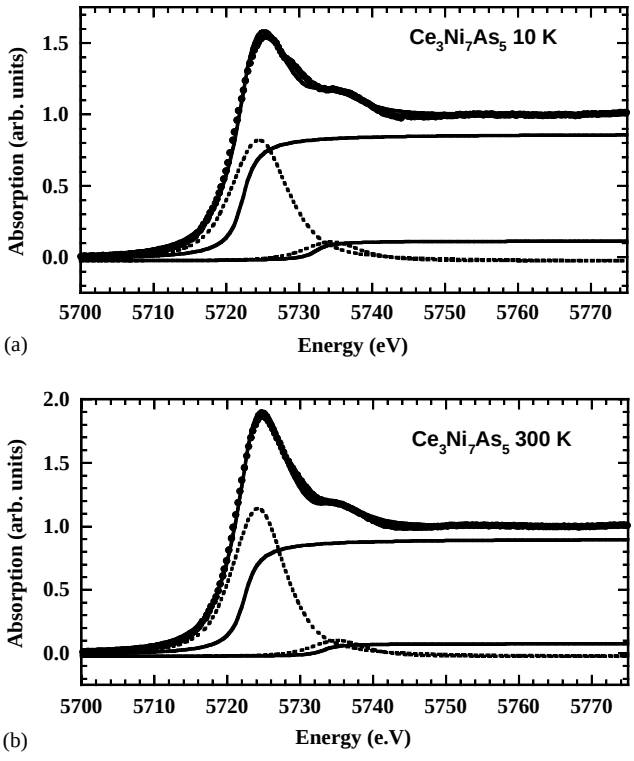

Fig. 10. X-ray absorption spectra recorded at the L_{III} edge in $Ce_3Ni_7As_5$ at $T = 10\,K$ (a) and at room temperature (b). The points correspond to the measured data and the continuous line is a fit to the experimental data. The corresponding model decompositions into $4f^1$ and $4f^0$ contributions are also shown in the lower part of the figures.

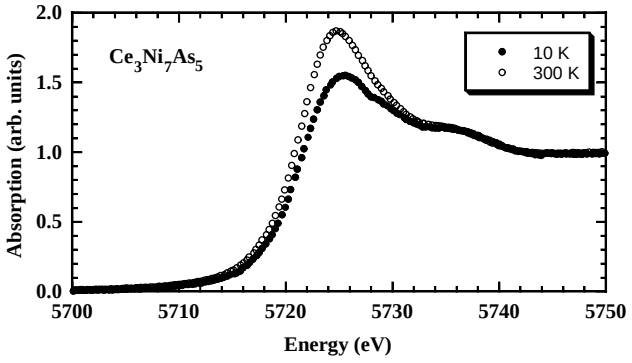

Fig. 11. Cerium L_{III} edge at 10 K (filled circles) and at room temperature (open circles) for $Ce_3Ni_7As_5$.

have fitted the observed spectrum using a deconvolution technique described in detailed elsewhere [45–47]. The fit of the Ce L_{III} absorption edge in $Ce_3Ni_7As_5$ recorded at 10 and 300 K data are plotted in Fig. 10. The presence of two configurations $4f^0$ and $4f^1$ bears witness of the existence of an intermediate valence state of the cerium atom in $Ce_3Ni_7As_5$. The Ce valence state is found to be $v = 3.10$ and 3.14 at room temperature and 10 K, respectively. An interesting feature of $Ce_3Ni_7As_5$ is the thermal dependence of the Ce valence state. A

comparison of the 10 and 300 K absorption edges (Fig. 11) clearly shows that the low energy peak, which occurs at ca. 5725 eV, increases upon heating. This shows a relocalization of the 4*f* electronic orbitals. This relocalization is partial since a pure trivalent state is not reached. This valence change can not be induced by a magnetic order at low temperature since Ni does not carry any magnetic moment and Ce is clearly in an intermediate valence state and consequently no 4*f* magnetic moment is expected on the Ce atoms. The origin of this partial relocalization of the 4*f* states most probably originates from structural changes such as a thermal change of the lattice parameters. Indeed, the expected thermal variation of the lattice parameters could favor an evolution of the bonds of Ce with its neighbors.

It is worthwhile to note that the intermediate valence state of Ce obtained from X-ray absorption spectroscopy is in excellent agreement with the results of the magnetic properties (vide supra). A similar valence state has recently been reported in other Ce–Ni–X phases where *X* is a non-metal atom: $Ce_2Ni_{15}Si_2$ [48], $Ce_2Ni_{17}Si_9$ [49] and $Ce_{20}Ni_{42}As_{31}$ [50]. In $Ce_3Ni_7As_5$, the Ce atoms are located in two crystallographically non-equivalent sites, each of them may not carry the same valence state. Consequently, the valence state of Ce deduced from X-ray absorption spectroscopy has to be taken as mean average value over these two non-equivalent Ce sites. The valence state of Ce is known to be closely related to its nearest neighbor environment. In some compounds such as $Ce_3Ni_2Ge_7$ [51], only one out of the two cerium sites has been found to carry an ordered magnetic moment. In $Ce_3Ni_7As_5$ it is not possible to differentiate the Ce valence state of the two Ce sites but the absence of any magnetic ordering and the pronounced intermediate valence character, observed at low temperatures, makes the hypothesis of one trivalent state very unlikely.

Concerning the environment of the Ce atoms in $Ce_3Ni_7As_5$ it is worthwhile to mention that Ce1 has the same number of As and Ni atoms as Ce4 in $Ce_{20}Ni_{41}As_{31}$, and that Ce2 in $Ce_3Ni_7As_5$ has also the same number and kind of neighbors as Ce3 in $Ce_{20}Ni_{41}As_{31}$ [50].

4. Conclusion

We have studied the structural and physical properties of the ternary phases $R_3Ni_7As_5$ (*R* =La, Ce, Pr, Nd, Sm). In comparison, these arsenides are closely related with the phosphides $R_3Ni_7P_5$ (*R* =La, Ce, Pr, Nd, Sm, Gd, Tb), which, however, crystallize in another structure type with hexagonal symmetry, space group $P6_3/m$, the $Nd_3Ni_7P_5$ type, $a = 1.6679(8)$, $c = 0.3891(1)$ nm [52]. From X-ray single crystal structure data of $Ce_3Ni_7P_5$ a partial occupation of an additional position 6*h* around the sixfold axis of the hexagonal lattice by Ni atoms was deduced. Hence the correct formula for the Ce-containing phosphide is rather $Ce_6Ni_{15}P_{10}$ than $Ce_3Ni_7P_5$ [53].

In a previous paper on the Ce–Ni–As system [16], we have reported the existence of a new family of ternary rare-earth nickel arsenides $R_6Ni_{13.4}P_9$ (*R* =La, Ce, Nd). Preliminary X-ray studies let us consider a $BaAl_4$ derivative structure type with orthorhombic symmetry and possible space groups *I*222, *Imm*2 or *Immm*. The unit cell parameters for the Ce-containing arsenide ($a = 0.4136(8)$, $b = 1.2213(3)$, $c = 0.9641(2)$ nm) are slightly different from those found for $Ce_3Ni_7As_5$, which is particularly true for the *b* parameter. Consequently two structural modifications for $Ce_3Ni_7As_5$ might exist: one, presented in this paper, is related to the $CaBe_2Ge_2$ type, a second could be related to the $ThCr_2Si_2$ type as reported earlier for the stannide $Dy_3Co_6Sn_5$ [15]. Such a surmise must not be excluded, since the stoichiometric arsenide $CeNi_2As_2$ exists in two polymorphic forms, i.e., the $CaBe_2Ge_2$ and $ThCr_2Si_2$ types [54].

The resistivity versus temperature plot of the temperature independent Pauli paramagnet $La_3Ni_7As_5$ was used as a reference compound to describe the magnetic contribution ρ_{mag} to the total resistivity of the Ce containing compound. $Ce_3Ni_7As_5$ is a typical intermediate valence system, which does not show a magnetic transition down to 4 K. The X-ray absorption experiments prove the *f*-*d* hybridization effects at low temperatures. The strength of this hybridization is found to be much less at room temperature. It is worthwhile to mention, that the local environment of the Ce atoms is quite similar to the one in the related valence fluctuator $Ce_{20}Ni_{42}As_{31}$ [50]. The shape of the $\rho_{mag}(T)$ curve is reminiscent of the behavior of an intermetallic compound exhibiting an interplay between Kondo and crystal-field interactions. The influence of the crystalline field seems to play no important role for the temperature dependence of the spin disorder resistivity of the paramagnetic sample $Pr_3Ni_7As_5$, as well as in case of both ferromagnetically ordering compounds $Nd_3Ni_7As_5$ and $Sm_3Ni_7As_5$, respectively.

Acknowledgments

V.B. is grateful to the Centre National de la Recherche Scientifique (CNRS) in France (2002) and the Austrian Science Foundation (2000) for their support through research grants. The authors also thank T. Roisnel (Centre de Diffractométrie, Université de Rennes 1) for X-ray intensity data collection, J.C. Jegaden, O. Rastoix and J. Le Lannic (CMEBA, Université de Rennes 1) for their assistance in the SEM studies and electron probe microanalyses. O.I. wishes to thank the Laboratoire LURE for the use of

the synchrotron facilities (XAS 13 spectrometer) as well as A. Traverse for interesting discussions.

References

[1] K.R. Andress, E. Alberti, Z. Metallkd. 27 (1935) 126.
[2] Z. Ban, M. Sikirica, Acta Crystallogr. 18 (1965) 594.
[3] B. Eisenmann, N. May, W. Müller, H. Schäfer, Z. Naturforsch. 27b (1972) 1155.
[4] H.F. Braun, N. Engel, E. Parthé, Phys. Rev. B 28 (1983) 1389.
[5] M. Sirjak, P. Lejay, B. Chevalier, J. Etourneau, P. Hagenmuller, J. Less-Common Met. 105 (1985) 139.
[6] K. Hiebl, C. Horvath, P. Rogl, J. Less-Common Met. 117 (1986) 375.
[7] D. Kußmann, R. Pöttgen, U.C. Rodewald, C. Rosenhahn, B.D. Mosel, G. Kotzyba, B. Künnen, Z. Naturforsch. 54b (1999) 1155.
[8] G. Venturini, B. Malaman, B. Roques, J. Less-Common Met. 146 (1989) 271.
[9] B. Eisenmann, H. Schäfer, Z. Anorg. Allg. Chem. 403 (1974) 163.
[10] A Gordon, F.J. DiSalvo, R. Pöttgen, J. Alloys Compd. 228 (1995) 16.
[11] Yu. Grin, M. Ellner, B. Predel, K. Peters, J. Alloys Compd. 201 (1993) 209.
[12] V. Babizhetskyy, E. Le Für, J.Y. Pivan, R. Guérin, Z. Naturforsch. 57b (2002) 1359.
[13] S. Zemni, J. Vicat, B. Lambert, R. Madar, P. Chaudouet, J.P. Sénateur, J. Less-Common Met. 143 (1988) 113.
[14] J. Dünner, A. Mewis, M. Roepke, G. Michels, Z. Anorg. Allg. Chem. 621 (1995) 1523.
[15] R. Pöttgen, Z. Naturforsch. 50b (1995) 175.
[16] V. Babizhetskyy, C. Le Sénéchal, J. Bauer, S. Députier, R. Guérin, J. Alloys Compd. 287 (1999) 174.
[17] COLLECT: KappaCCD software, Nonius BV, Delft, The Netherlands, 1998.
[18] Z. Otwinowski, W. Minor, in: C.W. Carter Jr., R.W. Sweet (Eds.), Methods in Enzymology, Academic Press, New York, 1997.
[19] G. Cascarano, A. Altomare, C. Giacovaggo, A. Guagliardi, A.G.G. Moliterni, D. Siliqi, M.C. Burla, G. Polidori, M. Camalli, Acta Crystallogr. A 52 (1996) C.
[20] V. Petricek, M. Dusek, JANA 2000: Crystallographic Computing System for Ordinary and Modulated Structures, Institute of Physics, ASCR, Praha, Czech Republic.
[21] K. Brandenburg, "Diamond," Version 2.0 (1998).
[22] A. San Miguel, Physica B 177 (1995) 208.
[23] F. Laves, Theory of Alloy Phases, ASM, Cleveland, OH, 1956.
[24] G. Aminoff, Z. Kristallogr. 58 (1923) 203.
[25] E. Larsson, Arkiv. Kemi. 23 (1964) 335.
[26] C. Le Sénéchal, V. Babizhetskyy, S. Députier, J.Y. Pivan, R. Guérin, Z. Anorg. Allg. Chem. 627 (2001) 1325.
[27] M.T. Béal-Monod, J.M. Lawrence, Phys. Rev. B 21 (1980) 5400.
[28] B. Chevalier, P. Rogl, K. Hiebl, J. Etourneau, J. Solid State Chem. 107 (1993) 327.
[29] J.M. Lawrence, P.S. Riseborough, R.D. Parks, Rep. Prog. Phys. 44 (1981) 1.
[30] B.C. Sales, D.K. Wohlleben, Phys. Rev. Lett. 35 (1975) 1240.
[31] N.F. Mott, H. Jones, Theory of the Properties of Metals and Alloys, Oxford University Press, London, 1964.
[32] G. Grimvall, The Electron-Phonon Interaction in Metals, North-Holland, Amsterdam, 1981.
[33] T. Moriya, Spin Fluctuations in Itinerant Electron Magnetism, Springer, Berlin, 1985.
[34] M.S. Wire, J.D. Thompson, Z. Fisk, Phys. Rev. B 30 (1984) 5591.
[35] C. Geibel, S. Thies, D. Kaczorowski, A. Mehner, A. Grauel, B. Seidel, U. Ahlheim, R. Helfrich, K. Petersen, C.D. Bredl, F. Steglich, Z. Phys. B 83 (1991) 305.
[36] D. Wohlleben, B. Wittershagen, Adv. Phys. 34 (1985) 403.
[37] J.M. Fournier, E. Gratz, in: K.A. Gschneidner Jr., L. Eyring, G.H. Lander, G.R. Choppin (Eds.), Handbook on the Physics and Chemistry of Rare Earths, North-Holland Amsterdam, 1993, p. 409.
[38] A.J. Arko, M.B. Brodsky, W.J. Nellis, Phys. Rev. B 5 (1972) 4564.
[39] J. Kondo, Prog. Theor. Phys. Japan 32 (1964) 37.
[40] D. Pines, P. Noziers, The Theory of Quantum Liquids, Addison-Welley, New York, 1980.
[41] K.H. Fischer, Z. Phys. B 74 (1989) 475.
[42] K. Kadowaki, S.B. Woods, Solid State Commun. 58 (1986) 507.
[43] D. Malterre, Phys. Rev. B 43 (1991) 1391.
[44] D. Malterre, Solid State Commun. 69 (1991) 475.
[45] J. Röhler, J. Magn. Magn. Mater. 47 (1985) 175.
[46] J. Röhler, in: K.A. Gschneider Jr., L. Eyring, S. Hufner (Eds.), Handbook on the Physics and Chemistry of Rare Earths, Vol. 10, Elsevier, Amsterdam, 1987.
[47] O. Isnard, S. Miraglia, K.H.J. Buschow, J. Synchrotron Radiat. 6 (1999) 703.
[48] O. Isnard, K.H.J. Buschow, J. Alloys Compd. 267 (1998) 50.
[49] O. Isnard, S. Miraglia, K.H.J. Buschow, Physica B 239 (1997) 365.
[50] V. Babizhetskyy, C. Le Sénéchal, R. Guérin, O. Isnard, K. Hiebl, Phys. Rev. B 66 (2002) 014102.
[51] L. Durivault, F. Bourée, B. Chevalier, G. André, J. Etourneau, O. Isnard, J. Magn. Magn. Mater. 232 (2001) 139.
[52] S. Chikhrij, S. Oryshchyn, Yu. Kuz'ma, T. Glovyak, Sov. Phys. Crystallogr. 34 (1989) 681.
[53] V. Babizhetskyy, S. Chikhrij, S. Oryshchyn, Yu. Kuz'ma, Ukr. Khim. Zh. 59 (1993) 240.
[54] E.H. El Ghadraoui, J.Y. Pivan, R. Guérin, O. Pena, J. Padiou, M. Sergent, Mater. Res. Bull. 23 (1988) 1345.